GEOPHYSICS, VOL. 84, NO. 6 (NOVEMBER-DECEMBER 2019); P. B363–B373, 11 FIGS., 2 TABLES.
10.1190/GEO2018-0588.1

Case History

Application of a convolutional neural network in permeability prediction: A case study in the Jacksonburg-Stringtown oil field, West Virginia, USA

Zhi Zhong[1], Timothy R. Carr[2], Xinming Wu[3], and Guochang Wang[4]

ABSTRACT

Permeability is a critical parameter for understanding subsurface fluid flow behavior, managing reservoirs, enhancing hydrocarbon recovery, and sequestering carbon dioxide. In general, permeability is measured in the laboratory based on subsurface core samples, calculated from well logs or estimated from well tests. However, laboratory measurements and well tests are expensive, time-consuming, and usually limited to a few core samples or wells in a hydrocarbon field or carbon storage site. Machine-learning techniques are good options for generating a rapid, robust, and cost-effective permeability prediction model because of their strengths to recognize the potential interrelationships between input and output variables. Convolutional neural networks (CNN), as a good pattern recognition algorithm, are widely used in image processing, natural language processing, and speech recognition, but are rarely used with regression problems and even less often in reservoir characterization. We have developed a CNN regression model to estimate the permeability in the Jacksonburg-Stringtown oil field, West Virginia, which is a potential carbon storage site and enhanced oil recovery operations field. We also evaluate the concept of the geologic feature image, which is converted from geophysical well logs. Five variables, including two commonly available conventional well logs (the gamma rays [GRs] and bulk density) and three well-log-derived variables (the slopes of the GR and bulk density curves, and shale content), are used to generate a geologic feature image. The CNN treats the geologic feature image as the input and the permeability as the desired output. In addition, the permeability predicted using traditional backpropagation artificial neural networks, which are optimized by genetic algorithms and particle swarm optimization, is compared with the permeability estimated using our CNN. Our results indicate that the CNN regression model provides more accurate permeability predictions than the traditional neural network.

INTRODUCTION

Absolute permeability k is a measurement of the ability of porous media (e.g., subsurface rock) to allow hydrocarbons, CO_2, and other viscous fluids to flow through it in the presence of one or multiple fluid phases (e.g., oil, gas, and formation water) (Berkowitz, 2002). Accurate prediction of the permeability is important for reservoir characterization, fluid migration analysis, enhancement of oil recovery, well placement optimization, field development, secure design of CO_2 sequestration, and safe management of radioactive waste disposal (Helle et al., 2001; Ahmadi et al., 2013; Zhong and Carr, 2019). Laboratory core measurements are a good approach to directly measure the permeability if subsurface core samples are available. However, this method is time-consuming and cost-intensive (Wu, 2005).

Different correlations have been proposed in the literature for permeability prediction. The Kozeny-Carman relationship, based on a tube-like model (Kozeny, 1927; Carman, 1937, 1956), can be used to calculate the permeability by using the porosity and the Kozeny

Manuscript received by the Editor 7 August 2018; revised manuscript received 2 July 2019; published ahead of production 14 August 2019; published online 09 October 2019.
[1]West Virginia University, Department of Geology and Geography, Morgantown, West Virginia 26506, USA and The University of Texas at Austin, Bureau of Economic Geology, Austin, Texas 78713, USA. E-mail: zhi.zhong@beg.utexas.edu.
[2]West Virginia University, Department of Geology and Geography, Morgantown, West Virginia 26506, USA. E-mail: tim.carr@mail.wvu.edu.
[3]University of Science and Technology of China, School of Earth and Space Sciences, Hefei, China. E-mail: xinmwu@ustc.edu.cn (corresponding author).
[4]Saint Francis University, Department of Petroleum and Natural Gas Engineering, Loretto, Pennsylvania 15940, USA. E-mail: gwang@francis.edu.

constant (Paterson, 1983; Walsh and Brace, 1984). However, the results are unreliable due to the uncertainty of numerous parameters and the constraint conditions of unconsolidated and homogeneous porous media (Mauran et al., 2001). Morris and Biggs (1967) develop an empirical correlation to predict the permeability by using porosity and resistivity-based saturation. In the absence of core data, Timur (1968) proposes a relationship among the irreducible water saturation, porosity, and permeability. Extending Timur's model by adding the impact of minerals, Ahmed et al. (1991) introduce a dual water model to estimate the permeability value. However, the irreducible water saturation is related to the shale volume and grain size; thus, the results are not reliable in a complex heterogeneous or fractured reservoir. Granberry and Keelan (1977) illustrate the relationships among the permeability, water saturation, and porosity, but the water saturation calculation increases the permeability uncertainty. A logarithmic-linear relationship between the permeability and porosity is another approach to calculate the permeability if porosity data are available, but the results are not sufficiently precise in carbonate reservoirs with a high degree of heterogeneity (Ahmadi et al., 2013).

Geophysical well logs are widely available in almost every hydrocarbon field. Many researchers (Kapadia and Menzie, 1985; Ahmed et al., 1991; Bloch, 1991) develop the relationship between permeability and well logs. Sen et al. (1990) aim to use nuclear magnetic resonance logs calibrated by core samples to estimate the permeability. However, these studies only contribute to a better understanding of the factors controlling permeability. In addition to core measurements, well-log response correlations, and empirical models, well pressure transient testing, which includes the pressure buildup (Miller et al., 1950; Clark and Golf-Racht, 1985; Pan et al., 2016), drill stem testing (Bourdet et al., 1989; Xu et al., 2008; Kabir et al., 2011), and repeat formation testing (Stewart and Wittmann, 1979) are generic techniques to obtain the mean permeability values for the interval open to flow into the wellbore. However, well pressure transient testing is time-consuming and cost-intensive. It provides only limited permeability information in a few wells and cannot describe the degree of reservoir heterogeneity. Production history matching based on numerical reservoir simulation is another approach to provide permeability values (Fayazi et al., 2016), but the matched permeability still depends on the original permeability distribution of the static geologic model. Therefore, it is necessary to introduce a fast, cost-effective, and physically reasonable method to establish a highly accurate relationship between the available core measured permeability and geophysical well logs (Zhong and Carr, 2018).

The artificial neural network, which has been widely applied in the petroleum industry due to its strengths to generalize and perform nonlinear approximation, is a suitable technique for constructing a regression model to predict the permeability (Mohaghegh and Ameri, 1995; Huang and Williamson, 1996; Huang et al., 1996; Van der Baan and Jutten, 2000; Helle et al., 2001; Al Moqbel and Wang, 2011; Mohebbi et al., 2012). Rogers et al. (1995) apply a backpropagation artificial neural network (BP-NN) to establish a permeability regression model by using porosity logs as the input; Jamialahmadi and Javadpour (2000) show that a radial base function neural network (RBF-NN) provides good performance in permeability estimation; Tahmasebi and Hezarkhani (2012) propose a modular neural network for permeability prediction; Al-Anazi and Gates (2012) conclude that a support vector machine performs better than an artificial neural network by using gamma ray (GR), neutron porosity, sonic porosity, and bulk density well logs; and Bagheripour (2014) successfully uses a committee neural network to construct a permeability prediction model by using well logs.

Overfitting is always challenging when attempting to obtain a robust and stable artificial neural network. Dropout (Srivastava et al., 2014) and cross-validation (Zhang et al., 1999; Esteva et al., 2017) techniques are widely used to overcome overfitting. Moreover, evolutionary algorithms, including genetic algorithms (GAs) and particle swarm optimization (PSO), are used to locate the global optimized initial weights and biases of an artificial neural network to avoid overfitting and premature convergence (Fernández Martínez et al., 2012; Zhong and Carr, 2016; Zhong et al., 2018). Feature engineering methods, including linear discriminant analysis (LDS) (Yang and Yang, 2003; Liu and Gillies, 2016), partial least squares (PLS) (Sousa and Åberg, 2018), and principal component analysis (PCA) (Yi et al., 2015), are also effective approaches to extract useful features of input data to reduce overfitting. However, these methods lose some raw data during feature engineering. In this work, we introduce a convolutional neural network (CNN) that not only effectively extracts input features from geophysical well-log data but also avoids information loss during feature engineering.

The concept of the CNN was first introduced in the 1960s when Hubel and Wiesel (1962) study the neurons in locally sensitive and directional selection processes of the cortical cortex. Now, this network type forms the prototype of many machine-learning algorithms in various fields of science, especially in the areas of computer vision, pattern classification, image processing, and natural language processing. The most remarkable breakthroughs of the CNN have involved the computer program AlphaGo developed by Google DeepMind (Silver et al., 2016). Because the CNN avoids preprocessing and manual feature selection of images, all image information can be fed into the CNN without any information loss. Although CNNs are widely used for classification problems, few studies have focused on regression problems, and none of them have focused on the application of CNNs in geologic reservoir characterization.

We assume that the combination of different geophysical well logs (such as those describing GR, bulk density, resistivity, neutron porosity, and acoustic characteristics) can represent reservoir properties. If well logs are fed into traditional artificial neural networks (such as the BP-NN, MLP-NN, and RBF-NN), those well logs can be calculated independently at the first layer of the ANN because neurons within the same layer are not interconnected. In the real world, well logs represent different physical phenomena/properties, and each of these phenomena may interact with or be affected by others. Therefore, the combination of well logs at any depth can represent one reservoir property at the corresponding depth, and this reservoir property can be represented only by a combination of well logs. Such a combination of well logs is called a geologic feature image.

In this work, we first present the design of the CNN and then demonstrate its performance in training a permeability regression model. Although the geographic region in which our proposed method is applied is the Jacksonburg-Stringtown oil field in West Virginia, USA, the deep learning-based approach is generally applicable to other hydrocarbon reservoirs that require the use of quick and cost-effective permeability regression models. This paper is organized as follows. We briefly review the general CNN framework and introduce the concept of the geologic feature image in the methodology section. Then, we compare the permeability values predicted by various neural networks in the "Results" section. We discuss the interpretation of the geologic feature image in the "Discussion" section. The conclusions are provided in the last section.

METHODOLOGY

Convolutional neural network

The CNN is an important class of artificial neural networks, but independent of the traditional neural network (e.g., multilayer perception NN, RBF- NN, and fuzzy logic NN). The input data of the CNN have a grid-like topology, which can be regarded as a 1D, 2D, or 3D grid of pixels. Neurons in each convolutional layer are aligned in a 1D, 2D, or 3D format (depth, width, and length), respectively. The CNN combines three steps to realize pattern recognition, including local receptive fields, weight sharing, and undersampling. The local receptive field refers to the unit of each neural network layer. Only in a small neighborhood in the upper layer of the connection can each neuron extract the visual features of the primary, such as line segments, endpoints, and corners. Weight sharing refers to CNNs sharing some neuron weights; thus, fewer parameters are optimized during training. Undersampling can reduce the feature resolution of the displacement, magnification, and other forms of distortion invariance (Le and Borji, 2017; Zhong et al., 2019). Corresponding to three steps, a CNN is composed of convolutional layers, subsampling layers, and fully connected layers (Figure 1).

Convolutional layer

The convolutional layer is the basic layer in the CNN. The input of the convolutional layer is an $n \times m \times c$ array of pixel values, where n and m are the width and length of the image, respectively, and c is the depth/channel of the image. For an RGB image, $c = 3$, and for a black/white image, $c = 1$. Assume that a window covers a $k \times k \times c = 2 \times 2 \times 1$ area, overlaps the top left of an image, and scans across all the areas of this image (Figure 2a). This window is called the kernel (Figure 2a, top right) with a kernel size of $k \times k \times c$, and the region over which the window scans is called the receptive field (Figure 2a, top left). Note that the kernel depth in the first convolutional layer is the same as that of the input image. Therefore, the depth c of the kernel shown in Figure 2a is 1. As the kernel scans around the image, the pixel value of the kernel is multiplied by the pixel value of the original image, which is known as computing the elementwise multiplications. The summation of those products provides a single feature value, which is stored in feature maps at the specific location (Figure 2a, bottom). The kernel moves to the right by s units ($s = 1$ in Figure 2a) until arriving at the right edge, then moves to the downside by s units and so on, where s is the stride size. This process repeats at each pixel of the input image until the kernel scans all of the pixels of the input image. The final output is called a feature map (Figure 2a, bottom) (Nielsen, 2015), and its size is calculated by the following equation:

$$n_{\text{out}} = \frac{n + 2p - k}{s} + 1, \tag{1}$$

where n is the width/length of the input image, n_{out} is the width/length of the feature image, k is the size of the convolution kernel, p is the padding size, and s is the stride size.

Subsampling layer

The purpose of subsampling, also known as pooling, is to reduce the spatial size of the representation of the feature map generated in the convolution layer and to reduce the number of features and computational complexity of the network. After the features are extracted by the convolution layer, the pooling layer is used to merge

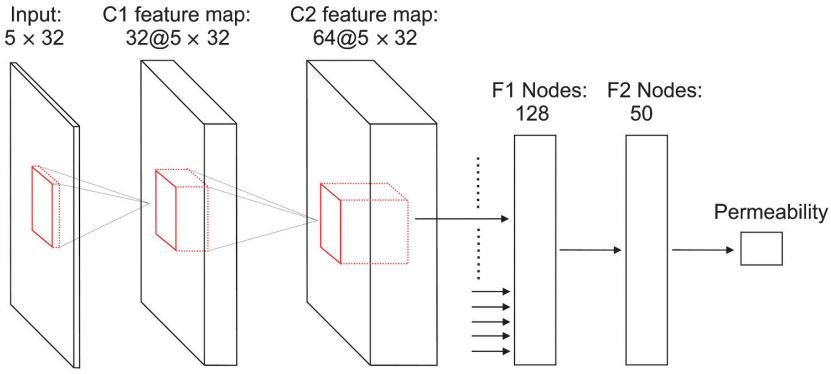

Figure 1. Schematic diagram of the CNN. Input layer: geologic feature image with a pixel size of 5×32. In this research, five well logs correspond to five geologic variables, and each variable is transformed into a 32-bit binary string. Convolution layer (C1): 32 5×32 feature maps that are generated by 32 kernels with a kernel size of 3×3 and with a stride of 2 and padding of 1. Convolution layer (C2): 64 5×32 feature maps that are generated by 64 kernels with a kernel size of 3×3, with a stride of 2 and padding of 1. Here, the depth of input for C2 is 32, which equals the number of kernels used in C1. Fully connected layers (F1): 10,240 nodes transformed from all pixels of C2, i.e., $64 \times 5 \times 32 = 10240$. The output layer (permeability) is fully connected with all nodes of F2, which has 50 nodes. Note that all of the activation functions in the CNN are ReLU functions, except the output layer, which is a linear activation function used to generate continuous values.

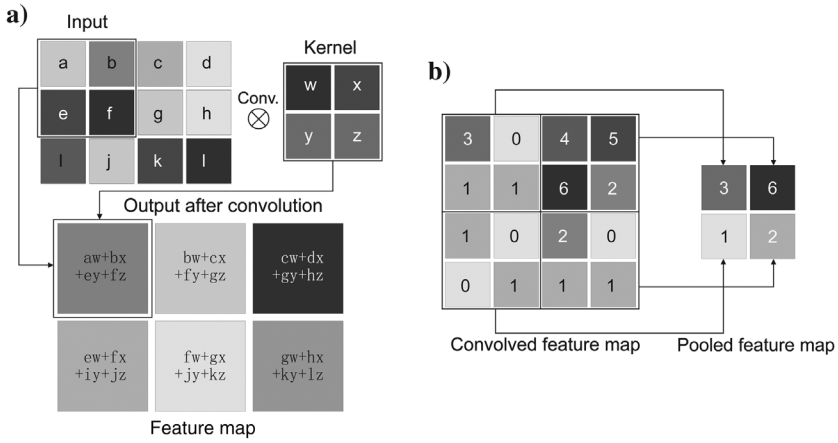

Figure 2. Schematic diagram of 2D convolution. (a) A 2×2 kernel convolves with a 3×4 image to produce a feature map (Goodfellow et al., 2016; Wang et al., 2017) and (b) max pooling: a 4×4 feature map is divided into four disjoint 2×2 regions and takes the maximum pixel value of each region to generate a 2×2 polled feature map.

similar features into a single one. The main reason for this step is to prevent the model from overfitting. The most commonly used pooling method is the max-pooling algorithm that returns the maximum value of nonoverlapping rectangular regions (see Figure 2b) (Wang et al., 2017). The size of the final pooled feature map is 1/4 of the previous convolution layer's feature map after subsampling computation. Owing to the convolution and pooling operation, the CNN can detect image features and recognize subtle differences among numerous pixel points (Wang et al., 2017).

Fully connected layer

After the features of the input image are extracted by the convolutional layers, they are fed into fully connected layers, which are appended to the end of the last convolutional layer. The output of the fully connected layer is either discrete values (for classification problems) or continuous values (for regression problems), which depends entirely on the specific research requirement. In this research, our desired output is the permeability, which is a continuous value.

In a practical system, there are several pairs of convolution and pooling layers. In this research, as Figure 1 shows, two convolution layers were used, and there is no pooling layer, which will be discussed in the "Discussion" section. In the first convolutional layer ($C1$), 32 3×3 kernels produce 32 feature maps; and in the second convolutional layer ($C2$), 64 $3 \times 3 \times 32$ kernels generate 64 feature maps. Note that the depth of the kernels, which is used in the second convolutional layer ($C2$), should be the same as the number of kernels used in the first convolutional layer ($C1$), which is 32. The output calculated by the second convolutional layer ($C2$) is flattened into a 1D vector and fed into the first fully connected layer ($F1$), which has $64 \times 5 \times 32 = 10{,}240$ neurons. The final output layer (permeability) is appended after the second fully connected layer ($F2$), which has 50 neurons.

Evolutionary algorithm optimized backpropagation neural network

To highlight the advantages and accurate performance of the CNN, a traditional BP-NN is introduced. The process of training a neural network involves tuning the values of the weights and biases of the neural network to minimize the error between the target and computed output. To avoid the network falling into local minima, two stochastic intelligence algorithms, namely, the GA and PSO, are used to optimize the initial weights and biases of the neural network by generating new offspring for the GA or changing the direction of movement and velocity for the PSO.

GAs were first proposed in the 1970s (Holland, 1992). This global heuristic search algorithm is based on Darwinian evolutionary theory, and it is inspired by biological evolution and natural genetics. Over the past several decades, GAs have attracted attention because of their potential as optimization techniques for complex functions. Another evolutionary algorithm used in this research is the PSO algorithm, which was introduced by Eberhart and Kennedy (1995). This algorithm imitates humans' (or insects') social behavior. Individuals interact with one another while learning from their own experience, and gradually, the population members move into better regions of the problem space.

In this research, the GA and PSO algorithms are used to search the suitable initial weights and biases of a BP-NN to improve the prediction performance and generalization and to overcome overfitting. For the detailed structure and workflow of these two algorithms, refer to Zhong (2017).

Table 1. Error measures for accuracy assessment to evaluate the model performance (Zhong, 2017).

Accuracy measure	Mathematical expression
Coefficient of determination R^2	$R^2 = 1 - \frac{\sum_{i=1}^{N}(y_i - \bar{y}_i)}{\sum_{i=1}^{N} y_i - \text{averg}(y_i)}$
Correlation coefficient γ	$\gamma = \frac{\sum_{i=1}^{N}(y_i - \bar{y}_i)(\hat{y}_i - \bar{\hat{y}}_i)}{\sum_{i=1}^{N}(y_i - \bar{y}_i)^2 \sum_{i=1}^{N}(\hat{y}_i - \bar{\hat{y}}_i)^2}$
Root mean square error (rms error)	$\text{rmserror} = \sqrt{\frac{1}{N}\sum_{i=1}^{N}(y_i - \hat{y}_i)^2}$
Average absolute error (AAE)	$\text{AAE} = \frac{1}{N}\sum_{i=1}^{N}\lvert y_i - \hat{y}_i \rvert$
Maximum absolute error (MAE)	$\text{MAE} = \max \lvert y_i - \hat{y}_i \rvert$

Performance evaluation

The correlation coefficient γ is an important parameter for evaluating the performance of CNNs. However, this approach is not sufficient to fully characterize a complex regression problem. Therefore, to verify the reliability and accuracy of our proposed CNN model, four additional statistical parameters were introduced as evaluation indices of the model performance (Zhong and Carr, 2016). These performance evaluation parameters include the coefficient of determination R^2, root mean square error (rms error), average absolute error (AAE), and maximum absolute error (MAE), as listed in Table 1. An R^2 (coefficient of determination) value of 1 indicates a perfect regression model, whereas an R^2 value of 0 indicates a completely random model (Oyerokun, 2003). Moreover, the rms error is used to evaluate the overall performance, whereas the AAE and MAE are used to determine the error range of the predicted results. A model with high γ and R^2 values and low rms error, MAE, and AAE values is considered to have good performance. The formulas for calculating each parameter are listed in Table 1

CASE STUDY

Geologic setting

The Jacksonburg-Stringtown field is situated along the axis of the Burchfield syncline in northwestern West Virginia (Figure 3). The primary or secondary producing reservoir unit is the Late Devonian Gordon Stray interval, which is contained within the middle to late Catskill deltaic complex (Catskill delta). The sedimentary deposition is interpreted to coincide with the heavy rainfall produced by the tropical climate and accelerated during the Middle and Late Devonian (Piotrowski and Harper, 1979; McBride, 2000; Blakey, 2005). In the area of the Jacksonburg-Stringtown field, Gordon Stray/Gordon intervals are interpreted to be shoreline and shore-face sandstone that occupied a broad structural trend at the time of maximum regression of the Acadian clastic wedge. Unlike modern oil and gas fields, the Jacksonburg-Stringtown oil field has predominately low-quality well-log data (i.e., GR, bulk density well logs) and highly limited high-quality data (core measured porosity and permeability data) for reservoir characterization. The sparse modern subsurface data

characteristic of supermature fields such as Jacksonburg-Stringtown can inhibit the development of a robust geologic model and effective evaluation of the CO_2 storage capacity.

Data acquisition

A model's stability and accuracy are largely dependent on the reliability of the training data. In this research, the data are extremely sparse, with only 93 samples from six wells in the Jacksonburg-Stringtown field. The cored wells' locations are marked in Figure 3. To construct a reliable CNN regression model, the input data were divided into two parts: training data and testing data. Data associated with five wells were used to train the CNN model, whereas the data from the remaining wells were used to evaluate the stability and accuracy of the well-trained CNN regression model. The input variables involve two conventional well logs (the GR and bulk density well log) and three derived variables (the slope of the GR data, the slope of the density, and the shale content). The permeability value is the desired output. To demonstrate the heterogeneity of the Gordon Stray/Gordon Formation and to display the chaotic status of the information in the available data, crossplots of the permeability versus each input variable are illustrated in Figure 4. It is clear that the relationship between each input variable and the permeability is nonlinear.

Image generation

As discussed previously, CNNs are a powerful method for image processing. In this work, discrete well-log variables were transformed into a black/white geologic feature image, and the geologic feature image was then fed into the CNN to train the regression model. The detailed process is given by the following steps.

1) Convert each well-log variable from a decimal number into a binary string, which is also called the feature string. The values of the different well-log variables are smaller than 1000; thus, a 32 bit length of a string is enough to represent all of the values of the well-log variables. Figure 5 shows the details of the conversion process. Figure 5a shows the value of each variable. Different well logs are marked with different colors to classify them more easily.
2) Transform the feature string into a black/white image (Figure 5b).
3) Stack those black/white feature images vertically into one whole image (Figure 5c).

The image generated by steps 1–3 is a combination of different well-log variables, and it is called a geologic feature image. Each geologic feature image at a specific depth corresponds to one permeability value (Figure 5d). Each decimal value can be uniquely represented by a binary string; thus, each geologic feature image can be uniquely represented by a black/white image. A geologic feature image uses the combination of multiple white and black features to represent a complex value. It represents the unique combination of well-log information. The reason why feature values are converted into geologic feature images is highlighted in the "Discussion" section.

The CNN regression model that we constructed in this work does not have a pooling layer. The purpose of pooling is to merge semantically similar features into one; however, feature images represent one geologic phenomenon, and none of these geologic phenomena will be the same as those in the real world. Thus, these feature images should not be merged; otherwise, some information will be lost.

Figure 6 shows an example of a geologic feature image. The left side of this figure shows the feature values (GR = 36.915, density = 2.479, $S_{gr} = 6.610$, $S_{den} = 0.042$, and $V_{sh} = 0.302$); and the right side of this figure shows the corresponding geologic feature image. Here, GR is the GR well log, S_{gr} is the GR slope, S_{den} is the density slope, and V_{sh} is the shale content.

Data normalization

To ensure that the CNN regression model has the best possible performance, the output variables (permeability) are normalized by the following:

$$X^{new} = \frac{\log_{10}(X) - \log_{10}(X_{min})}{\log_{10}(X_{max}) - \log_{10}(X_{min})}, \tag{2}$$

where X^{new} is the normalized input vector, X is the original input vector, X_{min} is the minimum value, and X_{max} is the maximum value.

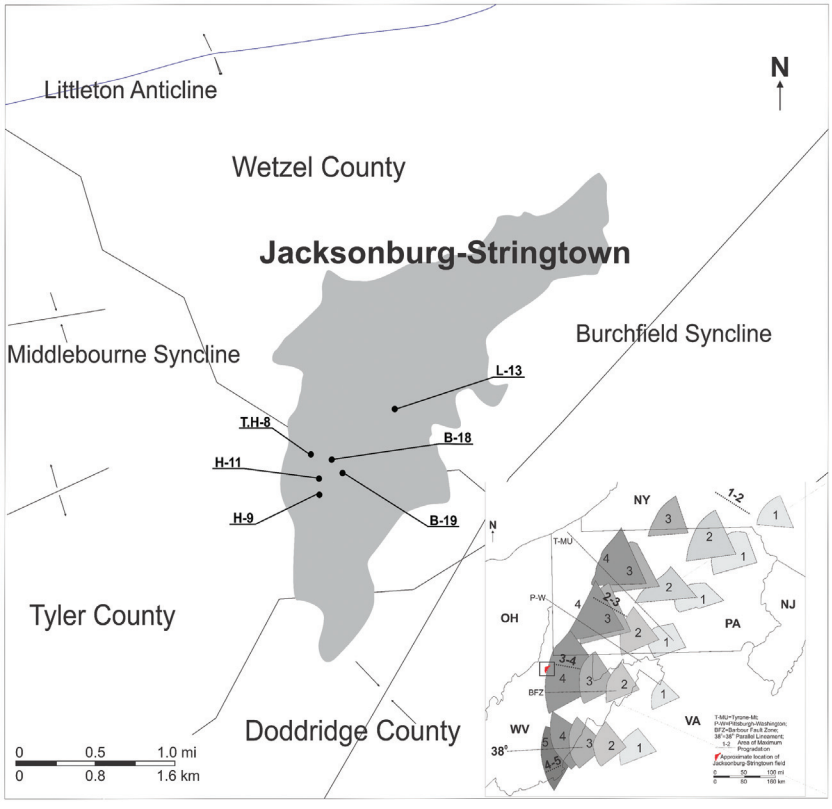

Figure 3. Location of the Jacksonburg-Stringtown oil field in northwestern West Virginia, which is marked by the black rectangular box in the thumbnail figure; the black dots mark the location of cored wells. The thumbnail figure shows the Late Devonian paleogeography in the Appalachian foreland basin.

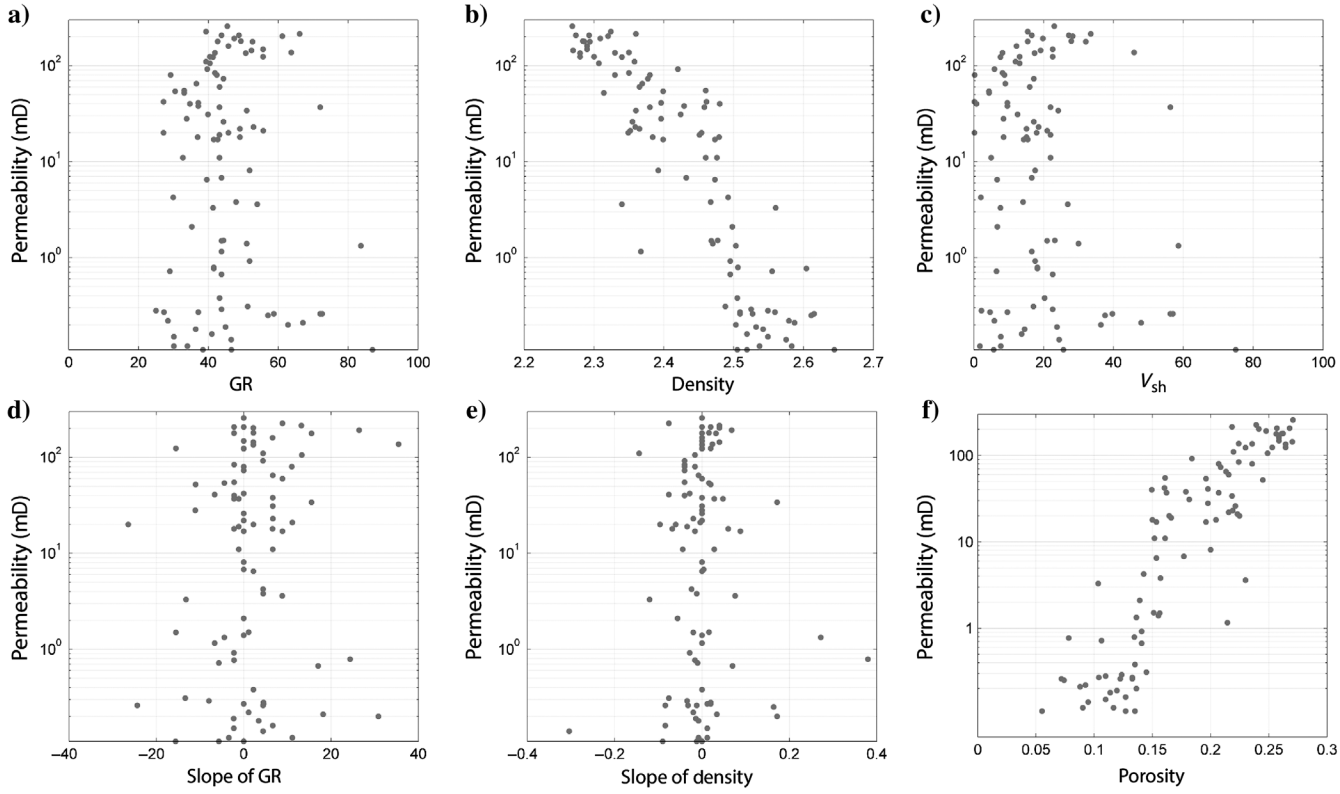

Figure 4. (a-e) Permeability versus different input variables that are used as input parameters in this study and (f) permeability versus porosity. It appears that there is no clear linear relationship between the permeability and each input variable.

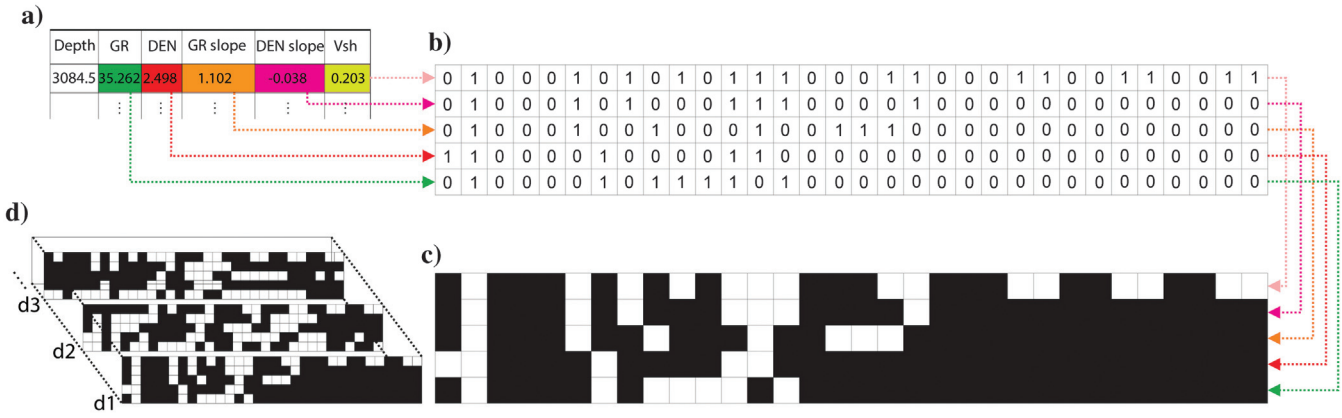

Figure 5. Schematic diagram of the data transform process. (a) Original data. (b) The 32bit string for each corresponding variable. All "1" values are replaced by 255, and "0" values are replaced by 0. (c) Convert the feature string (b) into a black/white image, and stack them to generate the geologic feature image. (d) Geologic feature images at different depths.

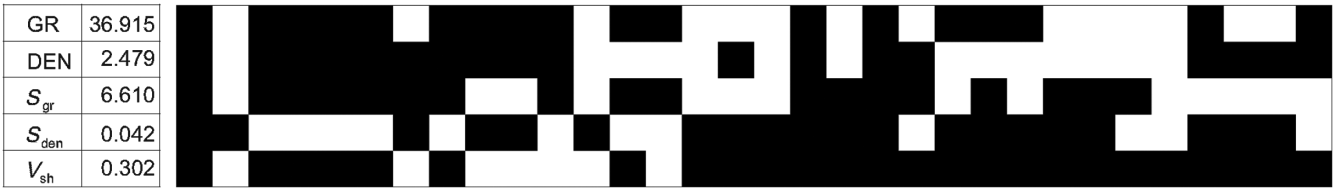

Figure 6. Example of a geologic feature image; the left table gives the specific values for different well-log variables, and the black/white image is the corresponding geologic feature image.

The normalized permeability X^{new} ranges from 0 to 1. The permeability values predicted by the well-trained CNN regression model should be reprojected into the original order by following the renormalization formula:

$$X^{\text{renormalized}} = 10^{(X_{\max}-X_{\min})X^{\text{predicted}}+X_{\min}}, \quad (3)$$

where $X^{\text{renormalized}}$ is the renormalized output and $X^{\text{predicted}}$ is the permeability predicted by the well-trained CNN model. The terms $X_{\min}$ and $X_{\max}$ are the minimum and maximum values in the trained target data, respectively, which are exactly the same as the values in equation 2.

RESULT

CNN result

To verify the generalization ability and stability of the CNN model, a well-trained CNN model is used to predict the permeability values in well B-19, from which the test data comprise 22 data points. The performance of the CNN in training and testing is listed in Table 2. According to Table 2, the R^2 value is 0.9676 for the training process and 0.9231 for the testing process, and the rms error is 114.7804 for the training process and 125.3144 for the testing process. Additionally, the MAE is 69.7293 for the training and testing processes. The average absolute error (AAE) is 5.2080 and 12.1739 for the training and testing data, respectively. All of these performance evaluation parameters indicate that the CNN has good generalization ability and stability.

Figure 7 shows the permeability profile of well B-19. The cyan dotted line in Figure 7 indicates the permeability predicted by using the well-trained CNN, and the blue dotted line is the core measured permeability. As Figure 7 shows, CNN can predict the permeability with high accuracy if the permeability values are greater than 1 mD, and the predicted results contain errors if the permeability values are smaller than 1 mD.

Figure 8 shows the crossplot of the permeability values measured in the laboratory and those predicted by using the CNN. The 45° diagonal line indicates perfect matching between the predicted permeability values and the true measured permeability values. As Figure 8 shows, the well-trained CNN can predict the permeability accurately if permeability is greater than 1 mD.

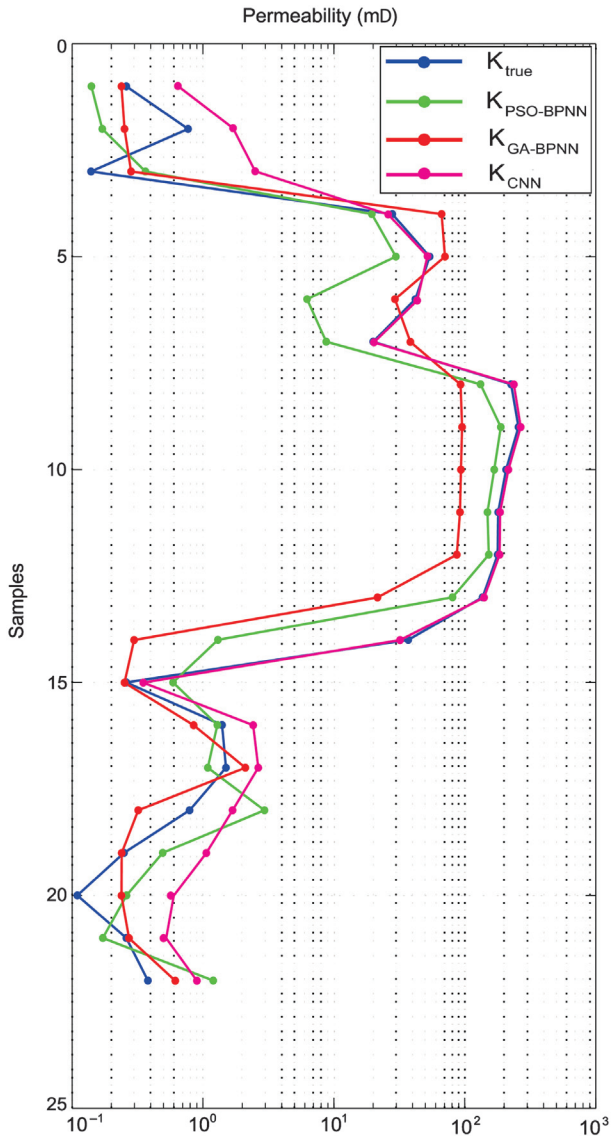

Figure 7. Well-log profile for test well B-19. The blue line indicates the core measured permeability; the green, red, and cyan lines indicate the permeability predicted by the PSO-BPNN, GA-BPNN, and CNN, respectively.

Table 2. Performance evaluation parameters of the different NNs for the training and testing processes.

Algorithm	Train/test	R^2	γ	rms error	MAE	AAE	ME	STD
CNN	Train	0.9676	0.9836	114.7804	69.7293	5.2080	3.7861	12.7740
BP-NN		0.9129	0.9555	162.8002	66.1630	7.0480	5.7862	19.5440
PSO-BP-NN		0.9588	0.9792	120.5960	79.5248	5.8631	5.0269	15.2930
GA-BP-NN		0.9254	0.9620	135.4920	57.3532	6.4628	4.9001	21.3520
CNN	Test	0.9231	0.9607	125.3144	69.7293	12.1736	−6.6101	24.3534
BP-NN		0.5177	0.7190	166.2519	128.3269	79.5620	28.5246	72.4190
PSO-BP-NN		0.9281	0.9595	137.5647	75.3279	25.3667	19.1389	26.6584
GA-BP-NN		0.8328	0.9126	158.9218	70.2500	30.5890	26.3529	60.8250

Comparing permeability predictions based on the various regression models

To further evaluate the performance of the CNN models, namely, BP-NN, GA -optimized BP-NN (GA-BP-NN), and PSO-optimized BP-NN (PSO-BP-NN) models, the permeability values predicted by different well-trained neural network models were compared with the available core measured permeability data.

Generally, the errors between the true permeability and the predicted permeability follow a normal distribution. Therefore, the mean μ and the standard deviations σ of errors are taken from a Gaussian model (Helle et al., 2001). Histograms and crossplots display the difference between the core measured permeability and the estimated permeability predicted by applying different neural networks based on the geophysical well logs (Figure 8). To compare the results more concisely, the permeability is plotted on a

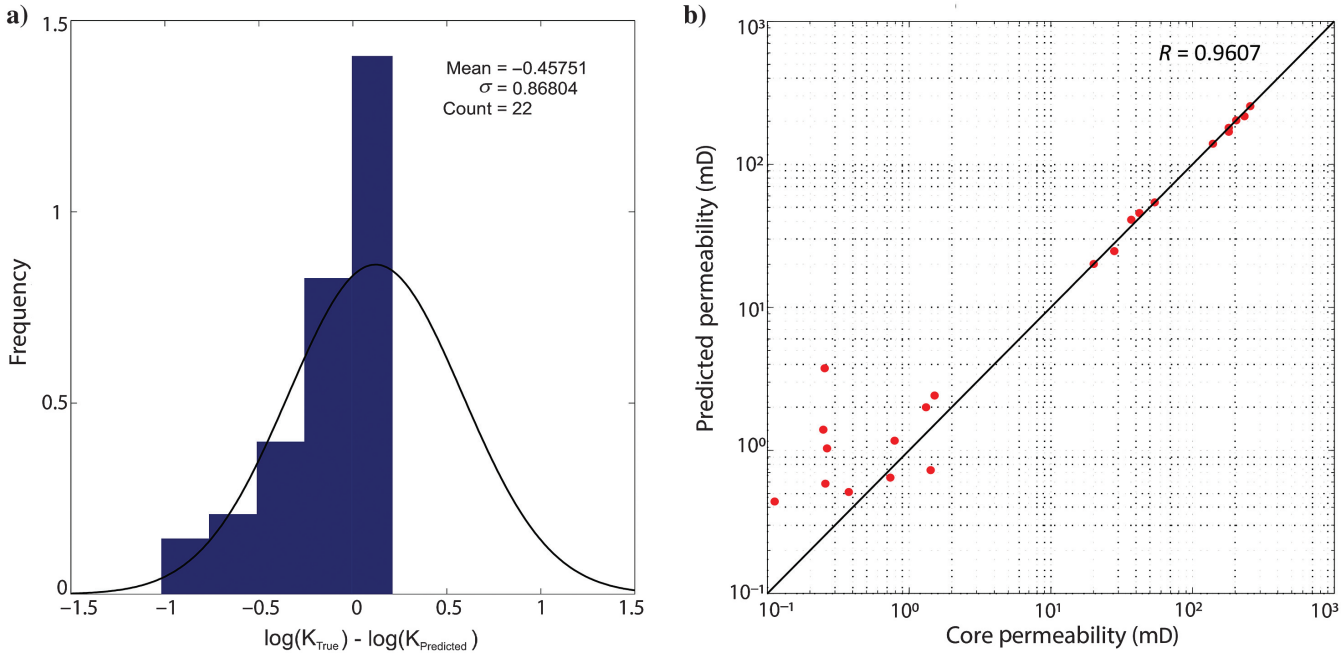

Figure 8. (a) Histogram of the error between the core measured permeability and the permeability predicted by using the CNN regression model. (b) The crossplot of the core measured permeability values and the permeability predicted by using the CNN regression model.

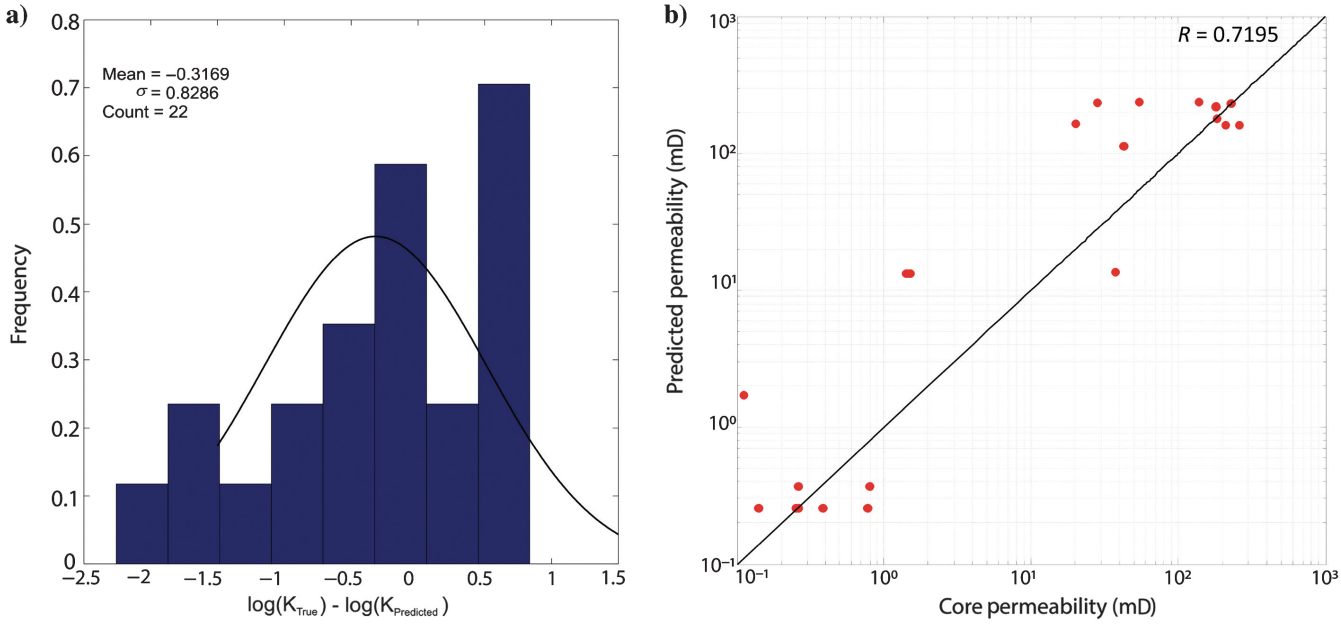

Figure 9. (a) Histogram of the error between the core measured permeability values and the permeability predicted by using the standard BP-NN model. (b) The crossplot of the core measured permeability values and the permeability predicted by using the standard BP-NN model.

logarithmic scale. A comparison between the core measured permeability and the permeability predicted by the CNN regression model shows a mean error μ of 6.6101 mD with a standard deviation σ of 24.3534 mD (Figure 8).

As Figure 9 shows, the mean error μ between the core measured permeability and the permeability predicted by the nonoptimized BP-NN is approximately 28.5246 mD with a standard deviation σ of 72.419 mD. The coefficient of determination R^2 and correlation coefficient r are 0.5177 and 0.7190, respectively. Comparing Figures 9 and 10, one can observe that the PSO-BP-NN performs better than the general BP-NN because the PSO-BP-NN has a low μ (19.438 mD) and low σ (26.6584 mD) and a high R^2 (0.9208) and high r (0.9596) (Figure 10). As shown in Figure 11, compared with the general BP-NN, the GA-BP-NN has a smaller mean error

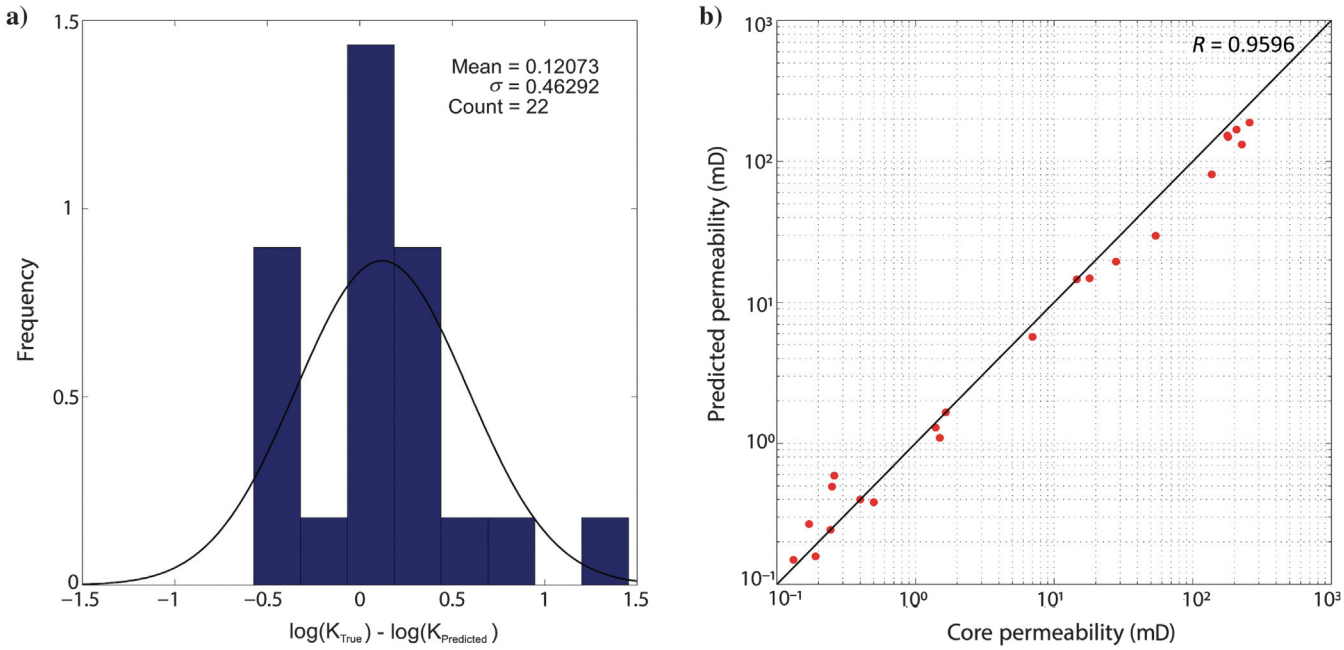

Figure 10. (a) Histogram of the error between the core measured permeability values and the permeability predicted by using the PSO-BP-NN model. (b) The crossplot of the core measured permeability values and the permeability predicted by using the PSO-BP-NN model

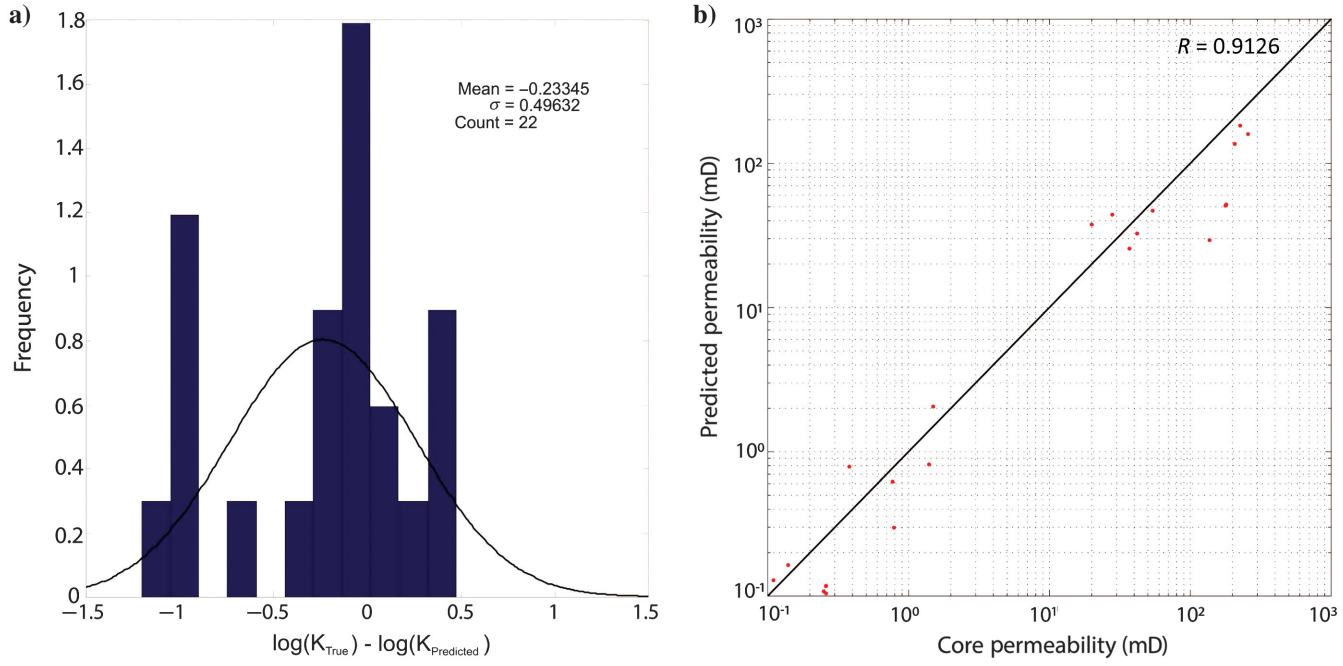

Figure 11. (a) Histogram of the error between the core measured permeability values and the permeability predicted by using the GA-BP-NN model. (b) The crossplot of the core measured permeability values and the permeability predicted by using the GA-BP-NN model

($\mu = 26.3259$), a smaller standard deviation ($\gamma = 60.825$), and a higher R^2 (0.8328) and r (0.9126).

The CNN provides a strong ability to predict the permeability with a high correlation coefficient, high coefficient of determination, and low mean square error among all regression models (Figure 8). The GA-BP-NN model has the same R^2 value as that of the PSO-BP-NN model, but the mean error value and standard deviation of the permeability predicted by the PSO-BP-NN model are lower. Therefore, the PSO-BP-NN provides a better prediction (Figure 11). The permeability predicted by the CNN, PSO-BP-NN, and GA-BP-NN and core measured permeability values are shown in Figure 7, which indicates a good agreement between the CNN results and the core measured permeability.

DISCUSSION

As shown in Figures 7 and 8, the CNN achieves better performance than the BP-NN and the evolutionarily optimized BP-NN. The input data provide some geophysical information regarding permeability. The GR log provides evidence of clay composition, which influences the permeability of the rock. The bulk density is inversely related to the porosity and shale content. The GR and bulk density slopes represent the change rate of the clay content. The shale content V_{sh} reflects the variation of the clay content in the rock. These input variables do not have any inner interaction in the traditional BP-NN because the neurons in each hidden layer are not connected. However, if input data are in the format of an image, the variables can communicate during the convolution calculation, as shown in Figure 5. Let us take the GR feature image and density feature image as an example. After the image is calculated by the convolutional kernels, new feature maps are generated, which contain partial information related to the GR and density data. In terms of geophysics, a high GR value indicates the rich presence of organic materials, commonly found in shale, whereas a low density can be indicative of nonshale lithology, including sandstone and carbonate. Therefore, the CNN works very well when it is applied to construct the relationship between the well-log data and the permeability.

However, as shown in Figures 5 and 6, the geologic feature map does not have any physical meaning or at least cannot reflect any real physical scene related to the permeability. The same limitation occurs in the computer vision and biology fields (Cang and Wei, 2017, 2018). To be sure, geologic feature images offer no interpretation from a human viewpoint, but for a machine, such images represent patterns. Thus, it is possible that a better image representation format of variables can be introduced in the future and that the geologic feature image can offer some physical insight.

CONCLUSION

Permeability is a critical parameter for hydrocarbon reservoirs and CO_2 storage site characterization. In this paper, we present a workflow for reservoir permeability prediction based on a CNN model. In the CNN model, five variables, including the GR value, density, GR slope, density slope, and V_{sh}, were selected as input parameters. The input variables were first converted into black/white geologic feature images and then fed into the CNN to train the regression model. Based on the performance of the CNN in blind testing, the CNN has a strong generalization ability for permeability prediction. To highlight the advantages of the CNN, two evolutionarily optimized BP-NNs are constructed to predict permeability. The permeability predicted by those BP-NNs is compared with the CNN's predicted permeability. The results prove that the CNN performed better than the GA-BP-NN, PSO-BP-NN, and standard BP-NN. In conclusion, converting geophysical well logs into geologic feature images is a useful method for the application of CNNs in permeability prediction. The geologic feature image is not interpretable from a geologic viewpoint; thus, more work needs to be done. Relative to the traditional BP-NN, the CNN was successfully applied to predict the permeability values and provide more accurate prediction results.

However, it should be noted that the well logs used in this research are limited by their availability. Different geophysical well logs, which generally include more geologic information reflecting more complicated petrophysical properties of rocks, can be used to characterize the reservoir properties by applying this proposed method.

ACKNOWLEDGMENTS

This work was funded in part by the US-China Clean Energy Research Center, Advanced Coal Technology Consortium, under grant no. DE-PI0000017 from the National Energy Technology Laboratory of the US Department of Energy.

DATA AND MATERIALS AVAILABILITY

Data associated with this research are available and can be obtained by contacting the corresponding author.

REFERENCES

Ahmadi, M. A., S. Zendehboudi, A. Lohi, A. Elkamel, and I. Chatzis, 2013, Reservoir permeability prediction by neural networks combined with hybrid genetic algorithm and particle swarm optimization: Geophysical Prospecting, **61**, 582–598, doi: 10.1111/j.1365-2478.2012.01080.x.

Ahmed, U., S. Crary, and G. Coates, 1991, Permeability estimation: The various sources and their interrelationships: Journal of Petroleum Technology, **43**, 578–587, doi: 10.2118/19604-PA.

Al-Anazi, A., and I. Gates, 2012, Support vector regression to predict porosity and permeability: Effect of sample size: Computers and Geosciences, **39**, 64–76, doi: 10.1016/j.cageo.2011.06.011.

Al Moqbel, A., and Y. Wang, 2011, Carbonate reservoir characterization with lithofacies clustering and porosity prediction: Journal of Geophysics and Engineering, **8**, 592–598, doi: 10.1088/1742-2132/8/4/011.

Bagheripour, P., 2014, Committee neural network model for rock permeability prediction: Journal of Applied Geophysics, **104**, 142–148, doi: 10.1016/j.jappgeo.2014.03.001.

Berkowitz, B., 2002, Characterizing flow and transport in fractured geological media: A review: Advances in Water Resources, **25**, 861–884, doi: 10.1016/S0309-1708(02)00042-8.

Blakey, R., 2005, Paleogeography and geologic evolution of North America: Northern Arizona University, http: jan.ucc.nau.edu/~rcb7/nam.html, accessed 15 March 2009.

Bloch, S., 1991, Empirical prediction of porosity and permeability in sandstones: AAPG Bulletin, **75**, 1145–1160.

Bourdet, D., J. Ayoub, and Y. Pirard, 1989, Use of pressure derivative in well test interpretation: SPE Formation Evaluation, **4**, 293–302, doi: 10.2118/12777-PA.

Cang, Z., and G.-W. Wei, 2017, TopologyNet: Topology based deep convolutional and multi-task neural networks for biomolecular property predictions: PLOS Computational Biology, **13**, e1005690, doi: 10.1371/journal.pcbi.1005690.

Cang, Z., and G.-W. Wei, 2018, Integration of element specific persistent homology and machine learning for protein-ligand binding affinity prediction: International Journal for Numerical Methods in Biomedical Engineering, **34**, e2914, doi: 10.1002/cnm.2914.

Carman, P. C., 1937, Fluid flow through granular beds: Transactions of the Institution of Chemical Engineers, **15**, 150–166.

Carman, P. C., 1956, Flow of gases through porous media: Academic Press Inc., 120–138.

Clark, D., and V. Golf-Racht, 1985, Pressure-derivative approach to transient test analysis: A high-permeability north sea reservoir example: Journal of Petroleum Technology, **37**, 2023–2039, doi: 10.2118/12959-PA.

Eberhart, R., and J. Kennedy, 1995, A new optimizer using particle swarm theory: Micro machine and Human Science: Proceedings of the Sixth International Symposium on IEEE, 39–43.

Esteva, A., B. Kuprel, R. A. Novoa, J. Ko, S. M. Swetter, H. M. Blau, and S. Thrun, 2017, Dermatologist-level classification of skin cancer with deep neural networks: Nature, **542**, 115–118, doi: 10.1038/nature21056.

Fayazi, A., H. Bagherzadeh, and A. Shahrabadi, 2016, Estimation of pseudo relative permeability curves for a heterogeneous reservoir with a new automatic history matching algorithm: Journal of Petroleum Science and Engineering, **140**, 154–163, doi: 10.1016/j.petrol.2016.01.013.

Fernández Martínez, J. L., T. Mukerji, E. García Gonzalo, and A. Suman, 2012, Reservoir characterization and inversion uncertainty via a family of particle swarm optimizers: Geophysics, **77**, no. 1, M1–M16, doi: 10.1190/geo2011-0041.1.

Goodfellow, I., Y. Bengio, and A. Courville, 2016, Deep learning: MIT Press, 128–156.

Granberry, R. J., and D. K. Keelan, 1977, Critical water estimates for Gulf Coast sandstone: Gulf Coast Association of Geological Societies Transactions, **27**, 41–43.

Helle, H. B., A. Bhatt, and B. Ursin, 2001, Porosity and permeability prediction from wireline logs using artificial neural networks: A North Sea case study: Geophysical Prospecting, **49**, 431–444, doi: 10.1046/j.1365-2478.2001.00271.x.

Holland, J. H., 1992, Adaptation in natural and artificial systems: An introductory analysis with applications to biology, control, and artificial intelligence: MIT Press, 28–45.

Huang, Z., J. Shimeld, M. Williamson, and J. Katsube, 1996, Permeability prediction with artificial neural network modeling in the Venture gas field, offshore eastern Canada: Geophysics, **61**, 422–436, doi: 10.1190/1.1443970.

Huang, Z., and M. A. Williamson, 1996, Artificial neural network modeling as an aid to source rock characterization: Marine and Petroleum Geology, **13**, 277–290, doi: 10.1016/0264-8172(95)00062-3.

Hubel, D. H., and T. N. Wiesel, 1962, Receptive fields, binocular interaction and functional architecture in the cat's visual cortex: The Journal of Physiology, **160**, 106–154, doi: 10.1113/jphysiol.1962.sp006837.

Jamialahmadi, M., and F. Javadpour, 2000, Relationship of permeability, porosity and depth using an artificial neural network: Journal of Petroleum Science and Engineering, **26**, 235–239, doi: 10.1016/S0920-4105(00)00037-1.

Kabir, A. H., S. McCalmont, T. Street, and R. L. Johnson, 2011, Reservoir characterization of Surat Basin coal seams using drill stem tests: Presented at the SPE Asia Pacific Oil and Gas Conference and Exhibition.

Kapadia, S., and D. Menzie, 1985, Determination of permeability variation factor V from log analysis: Annual Technical Conference and Exhibition, SPE, doi: 10.2523/14402-MS.

Kozeny, J., 1927, Über kapillare leitung der wasser in boden: Royal Academy of Science, **136**, 271–306.

Le, H., and A. Borji, 2017, What are the receptive, effective receptive, and projective fields of neurons in convolutional neural networks?: arXiv preprint arXiv:1705.07049.

Liu, R., and D. F. Gillies, 2016, Overfitting in linear feature extraction for classification of high-dimensional image data: Pattern Recognition, **53**, 73–86, doi: 10.1016/j.patcog.2015.11.015.

Mauran, S., L. Rigaud, and O. Coudevylle, 2001, Application of the Carman-Kozeny correlation to a high-porosity and anisotropic consolidated medium: The compressed expanded natural graphite: Transport in Porous Media, **43**, 355–376, doi: 10.1023/A:1010735118136.

McBride, P. S., 2000, Facies analysis of the Devonian Gordon stray sandstone in West Virginia: M.S. thesis, West Virginia University.

Miller, C., A. B. Dyes, and C. Hutchinson Jr, 1950, The estimation of permeability and reservoir pressure from bottom hole pressure build-up characteristics: Journal of Petroleum Technology, **2**, 91–104, doi: 10.2118/950091-G.

Mohaghegh, S., and S. Ameri, 1995, Artificial neural network as a valuable tool for petroleum engineers: Petroleum Computer Conference, SPE, 29220.

Mohebbi, A., R. Kamalpour, K. Keyvanloo, and A. Sarrafi, 2012, The prediction of permeability from well logging data based on reservoir zoning, using artificial neural networks in one of an Iranian heterogeneous oil reservoir: Petroleum Science and Technology, **30**, 1998–2007, doi: 10.1080/10916466.2010.518187.

Morris, R., and W. Biggs, 1967, Using log-derived values of water saturation and porosity: Presented at the SPWLA 8th Annual Logging Symposium.

Nielsen, M. A., 2015, Neural networks and deep learning: Determination Press, 59–118.

Oyerokun, A. A., 2003, A new approach for training and testing artificial neural networks for permeability prediction: M.S. thesis, West Virginia University.

Pan, F., B. J. McPherson, Z. Dai, W. Jia, S.-Y. Lee, W. Ampomah, H. Viswanathan, and R. Esser, 2016, Uncertainty analysis of carbon sequestration in an active CO_2-EOR field: International Journal of Greenhouse Gas Control, **51**, 18–28, doi: 10.1016/j.ijggc.2016.04.010.

Paterson, M., 1983, The equivalent channel model for permeability and resistivity in fluid-saturated rock reappraisal: Mechanics of Materials, **2**, 345–352, doi: 10.1016/0167-6636(83)90025-X.

Piotrowski, R. G., and J. Harper, 1979, Black shale and sandstone facies of the Devonian Catskill clastic wedge in the subsurface of western Pennsylvania: Technical report, Pennsylvania Department of Environmental Resources, Harrisburg (USA), Bureau of Topographic and Geologic Survey, 3–8.

Rogers, S., H. Chen, D. Kopaska-Merkel, and J. Fang, 1995, Predicting permeability from porosity using artificial neural networks: AAPG Bulletin, **79**, 1786–1796.

Sen, P., C. Straley, W. Kenyon, and M. Whittingham, 1990, Surface-to-volume ratio, charge density, nuclear magnetic relaxation, and permeability in clay-bearing sandstones: Geophysics, **55**, 61–69, doi: 10.1190/1.1442772.

Silver, D., A. Huang, C. J. Maddison, A. Guez, L. Sifre, G. Van Den Driessche, J. Schrittwieser, I. Antonoglou, V. Panneershelvam, and M. Lanctot, 2016, Mastering the game of Go with deep neural networks and tree search: Nature, **529**, 484–489, doi: 10.1038/nature16961.

Sousa, P. F. M., and K. M. Åberg, 2018, Can we beat overfitting? A closer look at Cloarec's PLS algorithm: Journal of Chemometrics, **32**, e3002, doi: 10.1002/cem.v32.6.

Srivastava, N., G. Hinton, A. Krizhevsky, I. Sutskever, and R. Salakhutdinov, 2014, Dropout: A simple way to prevent neural networks from overfitting: The Journal of Machine Learning Research, **15**, 1929–1958.

Stewart, G., and M. Wittmann, 1979, Interpretation of the pressure response of the repeat formation tester: Annual Technical Conference and Exhibition, SPE, doi: 10.2118/8362-MS.

Tahmasebi, P., and A. Hezarkhani, 2012, A fast and independent architecture of artificial neural network for permeability prediction: Journal of Petroleum Science and Engineering, **86**, 118–126, doi: 10.1016/j.petrol.2012.03.019.

Timur, A., 1968, An investigation of permeability, porosity, and residual water saturation relationships: Presented at the SPWLA 9th Annual Logging Symposium.

Van der Baan, M., and C. Jutten, 2000, Neural networks in geophysical applications: Geophysics, **65**, 1032–1047, doi: 10.1190/1.1444797.

Walsh, J. B., and W. Brace, 1984, The effect of pressure on porosity and the transport properties of rock: Journal of Geophysical Research: Solid Earth, **89**, 9425–9431, doi: 10.1029/JB089iB11p09425.

Wang, D., M. Zhang, J. Li, Z. Li, J. Q. Li, C. Song, and X. Chen, 2017, Intelligent constellation diagram analyzer using convolutional neural network-based deep learning: Optics Express, **25**, 17150–17166, doi: 10.1364/OE.25.017150.

Wu, T., 2005, Permeability prediction and drainage capillary pressure simulation in sandstone reservoirs: Ph.D. thesis, Texas A&M University.

Xu, L., J. Cai, S. Guo, P. Yi, D. Xiao, Y. Dai, S. Yang, C. Khong, G. Fujisawa, and C. Dong, 2008, Real time carbon dioxide quantification using wireline formation tester to optimize completion and drill stem testing decisions: SPE IPTC, 12081.

Yang, J., and J. Yang, 2003, Why can LDA be performed in PCA transformed space?: Pattern Recognition, **36**, 563–566, doi: 10.1016/S0031-3203(02)00048-1.

Yi, D., Z. Lei, and S. Z. Li, 2015, Shared representation learning for heterogenous face recognition: Automatic Face and Gesture Recognition, 11th IEEE International Conference and Workshops on, IEEE, 1–7.

Zhang, G., M. Y. Hu, B. E. Patuwo, and D. C. Indro, 1999, Artificial neural networks in bankruptcy prediction: General framework and cross-validation analysis: European Journal of Operational Research, **116**, 16–32, doi: 10.1016/S0377-2217(98)00051-4.

Zhong, Z., 2017, Storage capacity estimation of commercial scale injection and storage of CO_2 in the Jacksonburg-Stringtown Oil Field, West Virginia: Ph.D. thesis, West Virginia University.

Zhong, Z., and T. R. Carr, 2016, Application of mixed kernels function (MKF) based support vector regression model (SVR) for CO_2 — Reservoir oil minimum miscibility pressure prediction: Fuel, **184**, 590–603, doi: 10.1016/j.fuel.2016.07.030.

Zhong, Z., and T. R. Carr, 2018, Application of a new hybrid particle swarm optimization-mixed kernels function-based support vector machine model for reservoir porosity prediction: A case study in Jacksonburg-Stringtown Oil Field, West Virginia, USA: Interpretation, **7**, no. 1, T97–T112, doi: 10.1190/INT-2018-0093.1.

Zhong, Z., and T. R. Carr, 2019, Geostatistical 3D geological model construction to estimate the capacity of commercial scale injection and storage of CO_2 in Jacksonburg-Stringtown Oil Field, West Virginia, USA: International Journal of Greenhouse Gas Control, **80**, 61–75, doi: 10.1016/j.ijggc.2018.10.011.

Zhong, Z., S. Liu, M. Kazemi, and T. R. Carr, 2018, Dew point pressure prediction based on mixed-kernels-function support vector machine in gas-condensate reservoir: Fuel, **232**, 600–609, doi: 10.1016/j.fuel.2018.05.168.

Zhong, Z., A. Y. Sun, Q. Yang, and Q. Ouyan, 2019, A deep learning approach to anomaly detection in geological carbon sequestration sites using pressure measurements: Journal of Hydrology, **573**, 885–894, doi: 10.1016/j.jhydrol.2019.04.015.